Available online at www.sciencedirect.com
SCIENCE DIRECT®
International Journal of Heat and Fluid Flow 24 (2003) 512–519
International Journal of HEAT AND FLUID FLOW
www.elsevier.com/locate/ijhff

# Large eddy simulations of plane turbulent impinging jets at moderate Reynolds numbers

F. Beaubert *, S. Viazzo

*Ecole des Mines de Nantes, GEPEA UMR-CNRS 6144, 4 Rue A. Kastler, B.P. 20722, 44307 Nantes, France*

Received 30 November 2002; accepted 12 March 2003

**Abstract**

The flow field of plane impinging jets at moderate Reynolds numbers has been computed using large eddy simulation technique. Two Reynolds numbers ($Re = 3000$ and 7500) defined by the jet exit conditions are considered. Computations have been carried out using the dynamic Smagorinsky model. The simulations were performed to study the mean velocity, the turbulence statistics along the jet axis and at different vertical locations. The dynamics of the jet is explored using the instantaneous velocity, vorticity and low pressure fields with a focus on the impinging zone. The present results compare favorably to the experimental data available in the literature. The effect of the jet Reynolds number is significant between 3000 and 7500 both on the near and far field structure.


*Keywords:* Impinging jet; Turbulence; Large eddy simulation; Subgrid model

## 1. Introduction

Air curtain devices find their applications in fields as varied as food-industries, building energy saving, cold stores, fire protection and containments of polluted zones. Their functions are to limit the heat and mass transfers between two different climatic environments. If turbulent impinging jets have been the subject of a lot of experimental research works, they have been less studied by numerical simulations like DNS or LES. Classical statistical model like $k$–$\varepsilon$ have shown their limits for this problem: overestimation of the potential core, underprediction of the jet expansion, impinging zone poorly described. Craft et al. (1993) evaluated the performance of various turbulence models for the plane turbulent impinging jet but none of the models was able to yield satisfactory results. On the other hand, numerical simulations of the large turbulent scales (LES) seem a priori well adapted to this configuration insofar as the large, strongly energetic and anisotropic eddies are explicitly calculated. Recent large eddy simulations of a free plane turbulent jet have been performed by Dai et al. (1994) and Ribault et al. (1999). A few simulations have been performed for the plane turbulent impinging jet, we could quote the work of Hoffmann and Benocci (1994), Voke et al. (1995) and more recently the study of Cziesla et al. (2001).

The purpose of this study is to investigate the ability of large eddy simulation to predict the overall field quantities in the plane turbulent impinging jet. The considered configuration being that of an air blast acting like a separator and protector of atmosphere, we have been focused on the physical behavior of the turbulent plane jet in the vicinity of the impingement where most of the transfers are suspected to occur. The reduction of heat and mass transfers indeed requires a better understanding of the dynamics of the vortices present in the impinging zone. The dynamics of the jet is examined using instantaneous velocity, vorticity and low pressure fields. The LES results are compared to experimental data. An effect of Reynolds number is also discussed.

## 2. Mathematical formulation

The flow is governed by the three-dimensional time dependent incompressible Navier–Stokes and continuity equations which are written in primitive variables. In

* Corresponding author. Tel.: +33-02-51-858258; fax: +33-02-51-858299.
*E-mail address:* francois.beaubert@emn.fr (F. Beaubert).

0142-727X/03/$ - see front matter © 2003 Elsevier Science Inc. All rights reserved.
doi:10.1016/S0142-727X(03)00045-6

large eddy simulation, each variable of the flow $f$ is split into a *large anisotropic scale* component $\overline{f}$ (which is computed) and a small scale component $f'$ called *subgrid scale*, which is more isotropic and universal and have to be modeled. This separation is obtained by applying a spatial filter (indicated by an overbar) to the Navier–Stokes (Eq. (1)) and continuity (Eq. (2)) equations in order to reduce the amount of spatial scales to be solved. For incompressible flow, the space filtered equations can be written in the following non-dimensional form:

$$\frac{\partial \overline{u}_i}{\partial t} + \frac{\partial}{\partial x_j}(\overline{u}_i \overline{u}_j) = -\frac{\partial \overline{p}}{\partial x_i} - \frac{\partial \tau_{ij}}{\partial x_j} + \frac{1}{Re}\frac{\partial^2 \overline{u}_i}{\partial x_j \partial x_j} \tag{1}$$

$$\frac{\partial \overline{u}_i}{\partial x_i} = 0 \tag{2}$$

where the index $i = 1, 2, 3$ refers respectively to the $x$, $y$ and $z$ directions.

Here, all variables are non-dimensionalized by the maximum nozzle exit velocity $V_0$ on the jet axis and the nozzle width $e$. The Reynolds number is defined as $Re = V_0 e/\nu$ where $\nu$ is the kinematic viscosity. The subgrid scale stress $\tau_{ij}$ is expressed using the Leonard decomposition: $\tau_{ij} = \overline{u_i u_j} - \bar{u}_i \bar{u}_j$ and due to the divergence free constraint the pressure is modified according to: $\overline{P} = \overline{p^*} + \frac{1}{3}\tau_{kk}$ with $p^* = p/\rho$.

In this present work, the complex interactions between the resolved and unresolved scales are modeled using a turbulent eddy viscosity hypothesis. The anisotropic part of the subgrid scale stress $\tau_{ij}$ is linked to the eddy viscosity $\nu_\tau$ by the following expression:

$$\tau_{ij} - \frac{\delta_{ij}}{3}\tau_{kk} = -2\nu_\tau \bar{S}_{ij} \quad \text{with} \quad \nu_\tau = C\overline{\Delta}^2 |\bar{S}|$$
$$\text{and} \quad |\bar{S}| = \sqrt{2\bar{S}_{ij}\bar{S}_{ij}} \tag{3}$$

where $C$ is the dimensionless model coefficient, $\overline{\Delta} = (\Delta_x \Delta_y \Delta_z)^{1/3}$ the grid filter width and

$$S_{ij} = \frac{1}{2}\left(\frac{\partial \overline{u}_i}{\partial x_j} + \frac{\partial \overline{u}_j}{\partial x_i}\right)$$

the strain rate tensor.

The Smagorinsky model was tested as a first approach. The constant $C$ which is a priori fixed depends on the particular flow and different values have been proposed in the literature. We have chosen $C_s^2 = C = (0.12)^2$ (see Dai et al., 1994), a value which, although lower than the coefficient for isotropic turbulence, has been found to be better suited to shear flows. But this model has been rejected. In fact, it is too dissipative and predicts incorrect asymptotic behavior near a wall or in laminar zones and overpredicts the length of the potential core. Furthermore, it does not allow possible subgrid scale energy backscatter to the resolved scales. Ribault et al. (1999) reach the same conclusions and found that the subgrid dissipation given by the standard Smagorinsky model (with $C_s = 0.13$) is excessively high, resulting in a substantial underprediction of the jet width.

The dynamic Smagorinsky model which overcomes some of the drawbacks of the Smagorinsky model is a suitable alternative. Initially developed by Germano et al. (1991) to correct the excessive dissipation of the Smagorinsky model and modified by Lilly (1992), this model exhibits the correct asymptotic behavior near the walls and in laminar regions, and does not formally prohibit possible energy backscatter. The square of the constant $C_s^2$ is replaced by a coefficient $C_d$ which is dynamically computed and depends on the local structure of the flow. In order to compute $C_d$, a test filter denoted by a hat and of width larger than the grid filter is introduced. The dynamic constant is calculated with a least-squares approach according to:

$$C_d = -\frac{1}{2}\frac{[(L_{ij} - \frac{1}{3}L_{kk}\delta_{ij})M_{ij}]}{M_{ij}M_{ij}} \tag{4}$$

$$L_{ij} = \widehat{\overline{u}_i \overline{u}_j} - \widehat{\overline{u}}_i \widehat{\overline{u}}_j \tag{5}$$

$$M_{ij} = \widehat{\overline{\Delta}}^2 |\widehat{\bar{S}}| \widehat{\bar{S}}_{ij} - \bar{\Delta}^2 \widehat{|\bar{S}| \bar{S}_{ij}} \tag{6}$$

The model coefficient $C_d$ which is dynamically computed is a local and instantaneous quantity and thus can vary widely in time and space. However, this desirable property may lead to numerical instabilities caused by negative values of $C_d$. Accordingly, the numerator and denominator of Eq. (4) are averaged in the homogeneous direction. Furthermore, negative values of $\nu_\tau$ are clipped to zero if the total viscosity $\nu + \nu_\tau$ is negative. The test filter used in the dynamic Smagorinsky model is a symmetric discrete filter based on the trapezoidal rule:

$$\widehat{f_i} = \frac{1}{4}(f_{i-1} + 2f_i + f_{i+1}) \tag{7}$$

This filter is applied sequentially in each direction. The value of the ratio $\widehat{\overline{\Delta}}/\overline{\Delta}$ is fixed to $\sqrt{6}$, see Lund (1997), Najjar and Tafti (1996).

## 3. Numerical method

The computational domain is a rectangular box of dimensions $H_x \times H_y \times H_z$. The nozzle $e$ width is centered on the upper boundary of the computational domain (Fig. 1). Schiestel and Viazzo (1995) have previously found that non-staggered grids cannot prevent oscillatory numerical wiggles in the pressure field. In order to circumvent the pressure checkerboarding, a staggered MAC mesh is used. The convective terms are considered in the skew-symmetric form since their discrete analogues preserve the global conservation of momentum and kinetic energy on staggered mesh (in the inviscid limit).

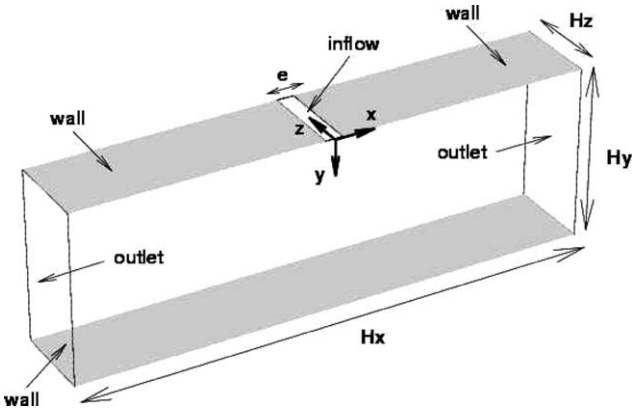


Fig. 1. Computational domain.

The spatial discretization is based on fourth order compact schemes in the inhomogeneous horizontal ($Ox$) and vertical ($Oy$) directions whereas Fourier pseudo-spectral methods are appropriate in the homogeneous transverse ($Oz$) direction.

The time advancement is second order accurate and is based on the explicit Adams–Bashforth scheme for the convective terms and the implicit Crank–Nicolson scheme for the viscous terms. The system of equations is solved using a two-step fractional scheme (*predictor–corrector*). At each time step, the problem reduces to a set of three Helmholtz equations (for the velocity components) and one Poisson equation (for the correction of pressure). The eddy viscosity depends both on time and space, so internal iterations are necessary for the resolution of the predictor step. Practically, three iterations are required to obtain a convergence criterion of $10^{-6}$.

At the exit of the jet, a constant (time invariant) inlet vertical velocity profile is used. This profile fits the mean nozzle exit velocity of previous experimental data obtained by Maurel et al. (2000). The same simulation with either a turbulent intensity of 10% at the nozzle exit or a fully developed constant inlet velocity profile has shown negligible effect on the turbulent statistics (Beaubert and Viazzo, 2001).

For the outflow regions a convective boundary condition is used to fix each component of the outflow velocity. This non-reflective boundary condition is based on the hyperbolic convection equation:

$$\frac{\partial u}{\partial t} + u_c \nabla u = 0 \tag{8}$$

The convective velocity $u_c$ is deduced from the instantaneous integrated mass flux through the outflow sections. Due to the presence of large vortices at the outflow boundaries, the reentries of fluid may cause an accumulation of instabilities at these locations. In order to prevent numerical instabilities on the outflow boundaries, a buffer domain of extent $5e$ is implemented (see Streett and Macaraeg, 1989/90).

A non-slip boundary condition is applied on the walls of the computational domain, whereas Neumann homogeneous conditions are used for the pressure correction. Periodic boundary conditions are appropriate in the homogeneous ($Oz$) direction.

## 4. Computational results

The present study is focused on the analysis of the statistical quantities (mean and rms quantities) along the jet axis and at different vertical locations. The dynamics of the impinging jet is also explored using the instantaneous velocity, vorticity and low pressure fields. The influence of the Reynolds number on the statistical quantities and the dynamics of the jet is also presented.

### 4.1. Computational details

Three different cases are computed to clarify the possible influence of the jet Reynolds number. The Reynolds number $Re = V_0 e/v$ is set to 3000 for case (I), 7500 for case (II) and 13 500 for case (III). The non-dimensional time step $\Delta t V_0/e$ is fixed to a value which ensure the stability of the numerical scheme (CFL < 0.3). For the largest Reynolds number simulation ($Re =$ 13 500), we have to mention that only first order statistics are here reported since insufficient integration times are yet available for this case.

The length of the horizontal direction must be large enough to capture the two large recirculations on each side of jet and to limit the influence of the buffer domain inside of the domain of interest. Preliminary bidimensional simulations have been used to test the influence of the length of the horizontal direction. We concluded that a value of $H_x/e = 40$ is sufficient. In the framework of air curtain applications, the opening ratio is fixed to 10 for all cases. The choice of the length of the homogeneous direction ($Oz$) is less obvious. Indeed, the periodic boundary conditions along the homogeneous direction are justified only if the transverse dimension $H_z$ is large enough to capture the largest structures of the flow. Consequently, the fluctuations must be practically decorrelated on a half-period ($H_z/2$). In the absence of two point correlations available in the literature for plane jets with short impingement distance, we considered successively two different transverse dimensions: $H_z/e = \pi$ in accordance with the simulations of Hoffmann and Benocci (1994), Voke et al. (1995), then a double dimension $H_z/e = 2\pi$. Note that Cziesla et al. (2001) set the length of the homogeneous direction to 2. Beaubert and Viazzo (2001) note an overlapping problem on the transverse two-point correlations of the different velocity components in the plane of symmetry of the jet for the smallest width. Therefore, a width of $2\pi$ for the transverse direction is rather advised for the ratio

Table 1
Computed cases

| Case | No. gridpoints | $\Delta x$ | $\Delta y$ | $\Delta z$ | $\Delta t V_0/e$ | $Re$ |
|---|---|---|---|---|---|---|
| I | $180 \times 160 \times 64$ | $2.52 \times 10^{-2}$–0.74 | $1.11 \times 10^{-2}$–0.1232 | $9.81 \times 10^{-2}$ | $3 \times 10^{-3}$ | 3000 |
| II | $240 \times 140 \times 64$ | $2.40 \times 10^{-2}$–0.90 | $5.44 \times 10^{-3}$–0.1659 | $9.81 \times 10^{-2}$ | $3 \times 10^{-3}$ | 7500 |
| III | $240 \times 150 \times 64$ | $2.40 \times 10^{-2}$–0.90 | $5.44 \times 10^{-3}$–0.1632 | $9.81 \times 10^{-2}$ | $1.75 \times 10^{-3}$ | 13500 |

$H_y/e = 10$ and in this range of Reynolds numbers. Table 1 contains the characteristics of the three simulations.

The grid spacing in the $(Ox)$ and $(Oy)$ directions is non-uniform to describe accurately the strong gradient regions with the grid points clustered near the wall and the two mixing layers around the jet axis. The grid is also refined near the detachment point of the wall jets to avoid too large anisotropic grid in this strong gradient region. We have, as far as possible, maintained an identical distribution of the grid points between the different cases but small adjustments have been necessary with increasing Reynolds number. In the homogeneous $(Oz)$ direction the mesh is uniform.

Long times of integration are required in order to ensure the statistical stationarity of the turbulent flow field. The averaging is performed in both time and the transverse homogeneous direction. Once statistical convergence is obtained, the statistics are calculated by averaging over the last 100 non-dimensional time units (for $Re = 3000$ and $Re = 7500$) defined as $T^* = TU_0/e$.

### 4.2. Mean flow and turbulence statistics

The mean and rms quantities are compared to experimental values of Maurel (2001) obtained for the same $H_y/e$ ratio and for a Reynolds number of 13 500 for the experiments.

In Fig. 2, the centerline $(x/e = 0)$ mean vertical velocity and the jet half width are reported and a good agreement with the experiment is obtained. This figure underlines the short length of the potential core for the smallest Reynolds number (case I). Furthermore, the length of the potential core is Reynolds dependent in the range of 3000–7500 (see Fig. 2). Above $Re = 7500$ the length of the potential core reaches a value around $4e$. For the jet half width $b_u/e$, a slight dependence on the Reynolds number is observed. This dependence increases with the difference of the slope of the mean vertical velocity profile along the jet axis, which is stronger for $y/e \geqslant 5$. For $Re = 7500$, the evolution of the jet half width is closed to the experiments of Browne et al. (1983) but for a free turbulent jet at $Re = 7620$.

The mean wall pressure (normalized by the maximum of pressure on the jet axis $p_i$) follows a gaussian distribution in accordance with the plane impinging jet experimental data of Tu and Wood (1996) in a range of Reynolds numbers between 6900 and 11 300 (see Fig. 3). The rms pressure plotted in the same figure exhibits two residual peaks located on either side of the jet axis. The wall shear stress is expressed as a skin friction coefficient defined by: $C_f = \tau_w/(0.5\rho V_0^2)$ for $y/e = 10$. The skin friction coefficient distribution along the impingement wall for $Re = 3000$ and $Re = 7500$ is shown in the same figure. The maxima of the friction coefficient are 0.12 and 0.086 respectively for $Re = 3000$ and $Re = 7500$. These values are in very good agreement with the experimental results of Tu and Wood (1996) obtained for the same ratio $H_y/e$ and for $Re = 3040$ and $Re = 6300$.

Fig. 4 shows the distribution of the vertical turbulence intensity $\langle v'^2 \rangle^{1/2}$ along the jet axis and the distribution of the Reynolds shear stress along the $x$-direction

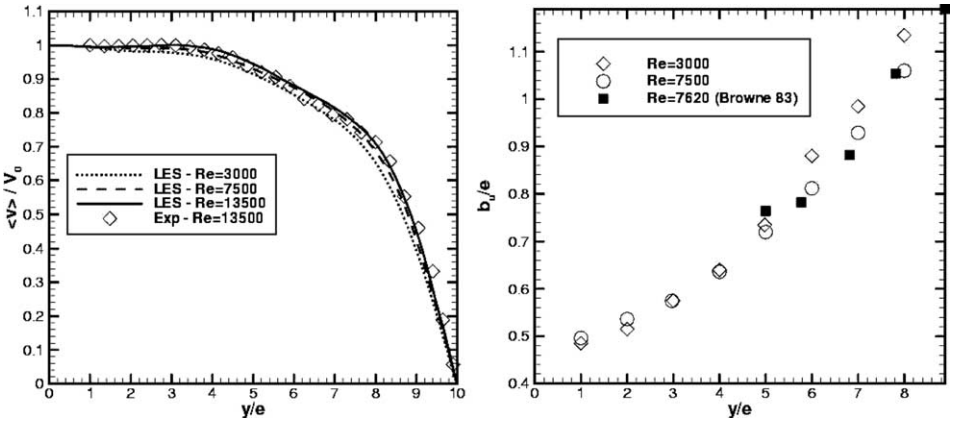


Fig. 2. Mean vertical velocity profiles along the jet axis—evolution of the jet half width $b_u$.

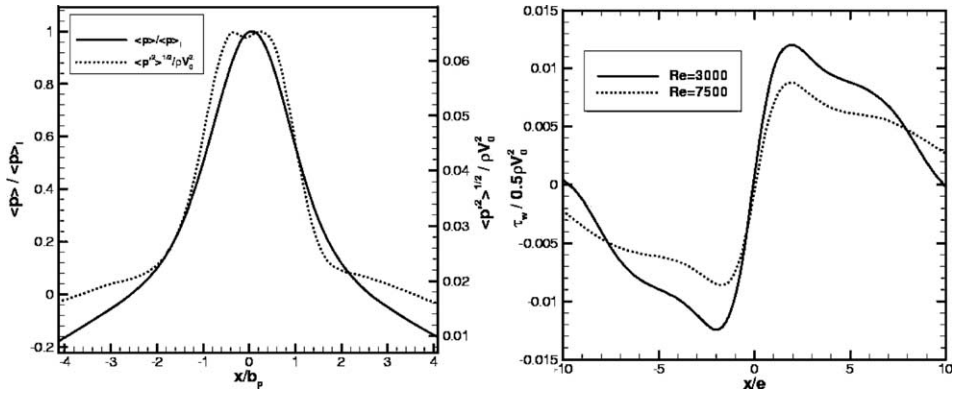


Fig. 3. Mean and rms wall pressure distribution for $Re = 7500$ (case II)—distribution of the skin friction coefficient along the impingement wall.

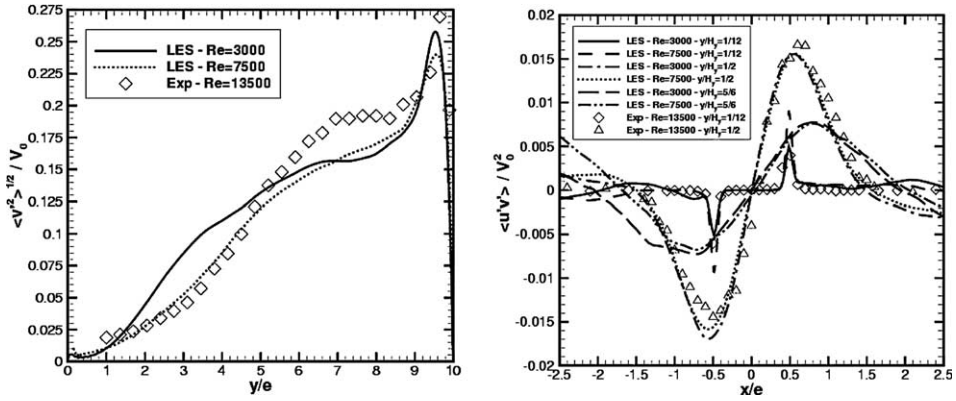


Fig. 4. Vertical turbulence intensity $\langle v'^2\rangle^{1/2}/V_0$ along the jet axis—horizontal distribution of the Reynolds shear stress.

for different $y$ locations. The peak of turbulence (around 25%) near the impingement is well described by the simulation. The slight discrepancy observed in the development zone of the jet for $Re = 3000$ is a Reynolds number effect: shorter length of the potential core and more organized structure of the flow in this zone for $Re = 3000$ (see Fig. 6). This peak is also observed for the other components of the turbulence intensity but closer to the impingement wall. For the horizontal turbulence intensity $\langle u'^2\rangle^{1/2}$ the peak is about two times smaller than the vertical component, whereas the magnitude of the transverse turbulence intensity $\langle w'^2\rangle^{1/2}$ is of the same order as the $\langle v'^2\rangle^{1/2}$ quantity. The Reynolds shear stress distribution along the $x$-direction is close to the experiments of Maurel (2001). The maximum values are located around the shear layer and no Reynolds number effect is observed. These results agree with the fact that small Reynolds number effects are suspected above $Re = 7500$.

### 4.3. Dynamics of the impinging jet

The dynamics of the impinging jet is explored using the instantaneous velocity, vorticity and low pressure fields, the effect of the Reynolds number on the flow structure is also studied. In order to clearly distinguish one of the two mixing layers, only one side of the jet is plotted in Fig. 5 which represents an isosurface of low pressure field for $0 \leqslant x/e \leqslant 1.5$ at $Re = 3000$ and 7500. The pressure is used here as tracer of swirling structures. It clearly reveals the presence of large bidimensional vortices generated by the shear-layer Kelvin–Helmholtz instabilities. The staggered pattern appears less organized with increasing Reynolds number.

The development of these structures can also be seen in Fig. 6 where the instantaneous vorticity norm is shown. In accordance with Husain et al. (1988), immediately downstream the nozzle the jet starts to develop symmetric vortices which are convected downstream. Secondary instabilities break them up and smaller scales emerge. Further downstream, the flow becomes fully turbulent as a broad spectrum of eddy sizes is formed. We also note (more pronounced for $Re = 3000$), in Figs. 5 and 6, the presence of intense vertical vortices typical of the mixing layers stretched between the former, see Comte et al. (1994). But the structure of the flow is quite different for $Re \geqslant 7500$: smaller and unorganized eddies are created closer to the nozzle (to clearly distinguish the differences in the flow

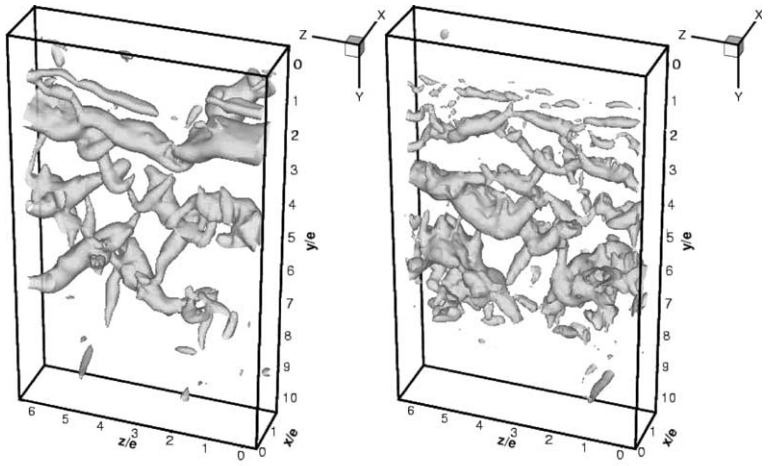


(a) Re=3000 with $p/\rho V_0^2 = -0.085$ (b) Re=7500 with $p/\rho V_0^2 = -0.045$

Fig. 5. Isosurface of low pressure.

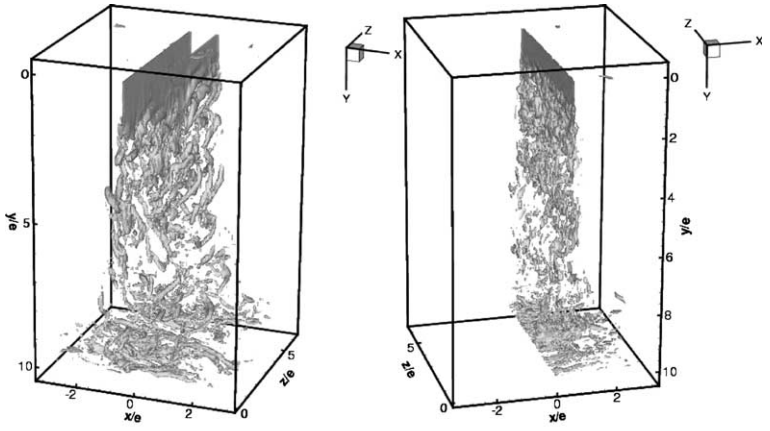


(a) Re=3000 with $\left(\omega_i^2\right)^{1/2} = 2.8$ (b) Re=7500 with $\left(\omega_i^2\right)^{1/2} = 2.8$

Fig. 6. Instantaneous field of the vorticity norm.

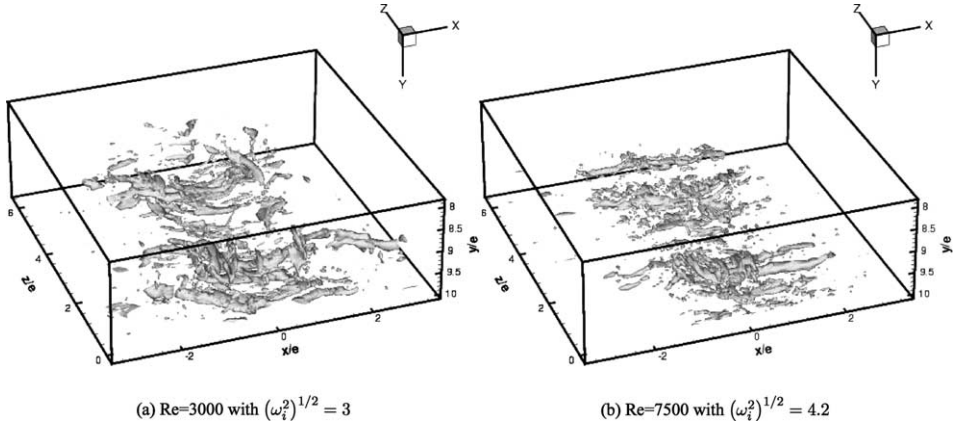


(a) Re=3000 with $\left(\omega_i^2\right)^{1/2} = 3$ (b) Re=7500 with $\left(\omega_i^2\right)^{1/2} = 4.2$

Fig. 7. Impinging zone—3D view of the counter-rotating cells.

structures only one side $(x/e \geqslant 0)$ of the two mixing layers is represented for $Re = 7500$).

In the impinging zone, strong three-dimensional effects appear. We can observe in Fig. 7 (3D view in the

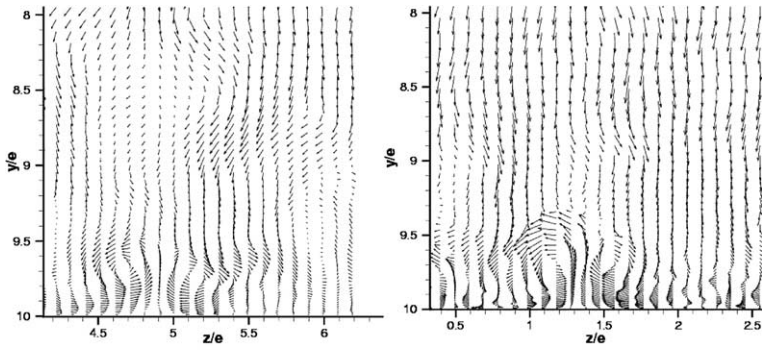


(a) Re=3000 at $x/e = -0.34$ (b) Re=7500 at $x/e = 0.512$

Fig. 8. Impinging zone—counter-rotating cells—slices in the ($yOz$) plane.

vicinity of the impinging zone) and Fig. 8 (slice in the ($yOz$) plane) the existence of time-dependent counter-rotating longitudinal vortices extending from both sides of the symmetry plane of the jet whose origins are not yet clearly established. These roll cells are often associated to Görtler vortices due to the streamline curvature near the impingement.

## 5. Conclusions

The present simulations of plane turbulent impinging jets enable the study of the dynamics of the vortices which is difficult to reach in experiments. It was also intended to develop a better understanding of the physics of the plane impinging jet to aid in deriving physically accurate closure models. The presence of counter-rotating cells near the impingement zone underlines the complexity of the flow. Those could play an important part in the process of transfer near the impingement plate as they extend on both sides of the symmetry plane of the jet. The statistical analysis reveals the influence of the Reynolds number on the jet structure between 3000 and 7500. Above this value the jet seems to have reached an asymptotic behavior which is also noticeable regarding the dynamics of the jet. Finally, when considering pseudo-spectral methods, the effect of the length of the homogeneous transverse direction is pointed out and must be checked carefully to retain reliable results.

## Acknowledgements

The calculations were carried out on the NEC-SX5 of the IDRIS center in Paris and at the computer science department of the Ecole des Mines de Nantes. The authors would like to thank R. Schiestel for the numerous and fruitful discussions as well as C. Solliec and S. Maurel for providing experimental results and valuable comments.

## References

Beaubert, R., Viazzo, S., 10–14 December 2001. Large eddy simulations of plane turbulent impinging jets. In: 14th Australasian Fluid Mechanics Conference. Adelaide University, Australia, pp. 425–428.

Browne, L.W.B., Antonia, R.A., Rajagopalan, S., Chambers, A.J, 1983. Interaction region of a two-dimensional turbulent plane jet in still air. In: Dumas, R., Fulachier, L. (Eds.), Structure of Complex Turbulent Shear Flow. pp. 411–419.

Comte, R., Ducros, F., Silvestrini, J., David, E., Lamballais, E., Métais, O., Lesieur, ML., 1994. Simulation des grandes échelles d'écoulements transitionnels. In: 74th Fluid Dynamics Symposium on Application of Direct and Large Eddy Simulation to Transition and Turbulence. Chania, Crete, Greece, pp. 14-1–14-12.

Craft, T., Graham, L., Launder, B., 1993. Impinging jet studies for turbulence model assessment, an examination of the performance of four turbulence models. Int. J. Heat Mass Transfer 36, 2685–2697.

Cziesla, T., Biswas, G., Chattopadhyay, H., Mitra, N.K., 2001. Large-eddy simulation of flow and heat transfer in an impinging slot jet. Int. J. Heat Fluid Flow 22, 500–508.

Dai, Y., Kobayashi, T., Taniguchi, N., 1994. Large eddy simulation of plane turbulent jet flow using a new outflow velocity boundary condition. JSME Int. J. 37 (2), 242–253.

Germano, M., Piomelli, U., Moin, R., Cabot, W.H., 1991. A dynamic subgrid-scale eddy viscosity model. Phys. Fluids A 3 (7), 1760–1765.

Hoffmann, G., Benocci, C., 1994. Numerical simulation of spatially-developing planar jets. In: 74th Fluid Dynamics Symposium on Application of Direct and Large Eddy Simulation of Transition and Turbulence, vol. 26. Chania, Crete, Greece, pp. 1–6.

Husain, H.S., Bridges, J.E., Hussain, F., 1988. Transport phenomena in turbulent flows. New York Hemisphere, Ch. Turbulence management in free shear flows by control of coherent structures, pp. 111–130.

Lilly, D., 1992. A proposed modification of the Germano subgrid-scale closure method. Phys. Fluids 4 (3), 633–635.

Lund, T., 1997. On the use of discrete filters for large eddy simulation. Annual Research Briefs—Center for Turbulence Research. pp. 83–95.

Maurel, S., 2001. Etude expérimental d'un jet plan en impact. Analyse parametrique et caracterisation des transferts de masse. Ph.D. thesis, Universite de Nantes, Nantes.

Maurel, S., Pavageau, M., Solliec, C., 2000. Parametric analysis of the impinging plane air jet on variable scaled-down models. In: 2000 ASME Fluids Engineering Conference, Boston.

Najjar, F., Tafti, D., 1996. Study of discrete test filters and finite difference approximations for the dynamic subgrid-scale stress model. Phys. Fluids 8 (4), 1076–1088.

Ribault, C.L., Sarkar, S., Stanley, S.A., 1999. Large eddy simulation of a plane jet. Phys. Fluids 11 (10), 3069–3083.

Schiestel, R., Viazzo, S., 1995. A Hermitian–Fourier numerical method for solving the incompressible Navier–Stokes equations. Comput. Fluids 24, 739–752.

Streett, C., Macaraeg, M., 1989/90. Spectral multi-domain for large-scale fluid dynamic simulations. Appl. Numer. Math. 26, 123–139.

Tu, C.V., Wood, D.H., 1996. Wall pressure and shear stress measurements beneath an impinging jet. Exp. Thermal Fluid Sci. 13, 364–373.

Voke, P.R., Gao, S., Leslie, D., 1995. Large-eddy simulations of plane impinging jets. Int. J. Numer. Methods Eng. 38, 489–507.